EES Catalysis

PAPER

View Article Online
View Journal

Cite this: DOI: 10.1039/d5ey00364d

Electric-field enhanced water-dissociation catalysis on oxide surfaces

T. Nathan Stovall,[ab] Justin C. Bui,[bcd] Yifan Wu,[bd] Shujin Hou,[bd] Shannon W. Boettcher *[abd] and Adam Z. Weber *[b]

Received 26th December 2025,
Accepted 5th January 2026

DOI: 10.1039/d5ey00364d

rsc.li/eescatalysis

Ion-transfer reactions in the presence of electric fields are ubiquitous in (bio/electro)chemical systems and catalysis, yet the impact of the electric field is poorly understood. Here, we use bipolar membranes (BPMs) to isolate electric-field-driven non-faradaic water dissociation (WD: $H_2O \rightarrow H^+ + OH^-$) on catalytic surfaces. We find the catalyst layer's ionic properties dictate both the transport and kinetic processes within the BPM. The role of these properties are explored *via* a series of membrane architectures, and catalyst poisoning experiments, and the corresponding current–voltage and impedance responses. Arrhenius analyses show that an acidic graphene-oxide (GO_x) catalyst layer gives rise to low interfacial H_2O entropy in the heterojunction, illustrated *via* a >100 fold increase in the Arrhenius prefactor relative to baseline TiO_2 measurements. Furthermore, ~50% of the applied driving force goes towards reducing the apparent enthalpic activation barrier in the case of GO_x, while other metal-oxide catalysts have enthalpic barriers independent of driving force. This analysis demonstrates a new mechanistic understanding of WD, where local electric fields augment enthalpic transition-state barriers, and the local ionic environment facilitates field-driven ion transfer. Ultimately, these results present a new design space for designing ion-transfer catalytic processes, and ionic heterojunctions more broadly.

Broader context

Bipolar membranes (BPMs) enable precise control of ionic fluxes and microenvironments. This, coupled with the unique ability to interconvert electrical and chemical potential, is poised to transform and realize a broad range of electrochemical technologies—including energy storage and conversion, chemical manufacturing, metal recovery, and advanced separations. Realizing this promise, requires understanding, and ultimately controlling, ionic (*e.g.*, transport and kinetic) processes within the bipolar membrane, a challenge that requires both fundamental and applied scientific insights. This work demonstrates how the BPM catalyst layer, and its acid–base properties, control both transport and kinetics through the BPM heterojunction. We also demonstrate how interfacial fields impact enthalpies and entropies of activation of thermochemical (*e.g.*, non-faradaic) ion transfer reactions and identify two regimes where either entropy or enthalpy is dominant. Beyond BPMs, most catalytic interfaces exist within highly polarized local microenvironments. Our demonstration of how electrostatics couple to entropies and enthalpies of activation informs how ultimately electrostatics can be leveraged to accelerate and optimize myriad catalytic processes.

1. Introduction

Electrified interfaces are central in driving heterogeneous electrocatalytic, as well as nominally "non-faradaic" catalytic processes.[1–11] Indeed, all heterogeneous catalysts undergo spontaneous charge transfer with their environment to equilibrate electrochemical potentials across the solid/liquid phase boundary. Likewise, active sites in biological systems, as in enzymes, have ligation environments that impart large local electric fields that are thought to promote reactivity.[12,13] During a chemical reaction (either formally faradaic or non-faradaic), the electric-potential gradient modulates the electrochemical potential of electrons and ionic species,[8] adsorbates,[14,15] and reorganizes solvent/solvation structures.[16] Catalytic reactions typically proceed *via* multi-step reaction mechanisms that may include charged species transiting the electric-potential gradient, bond cleavage, species (de)solvation, and specific interactions with the catalyst surface.[17–19] The rate of each of these

[a] Department of Chemistry University of California, Berkeley Berkeley, CA 94720, USA. E-mail: boettcher@berkeley.edu
[b] Energy Technologies Area Lawrence Berkeley National Laboratory Berkeley, CA 94720, USA. E-mail: azweber@lbl.gov
[c] Department of Chemical and Biomolecular Engineering NYU Tandon School of Engineering Brooklyn, NY 11201, USA
[d] Department of Chemical and Biomolecular Engineering University of California, Berkeley Berkeley, CA 94720, USA

steps can be impacted *via* the local electric-potential gradient; hence, even thermochemical processes long thought to be independent of potential have been recently shown to be strongly affected by local polarization,[4,9,20–23] for example electric fields increase the rate of alcohol dehydrogenation by orders of magnitude.[9] There remains much to understand regarding the underlying nature and field dependence of such processes and the role of the local electrostatic environment in defining reaction landscapes.

One of the simplest electric-field-enhanced reactions is the heterolytic dissociation of polar protic solvent molecules. Wien demonstrated that the conductivity of weak electrolytes (*e.g.*, H_2O) increases in the presence of transient electric fields and attributed the results to a field-driven increase in the dissociation constant.[24] Onsager provided a mathematical interpretation of these results, relating the dissociation constant to the electric field (a phenomena known as the Second-Wien Effect).[25] It is unclear how the results of Wien and Onsager, however, translate to traditional catalytic processes that proceed under a steady-state electric potential gradient and include interactions with a heterogeneous catalytic surface.

Bipolar membranes (BPMs) provide a platform to isolate the electric-field-dependent rate of nominally non-faradaic heterolytic water dissociation (WD, eqn (1)) under a steady-state electric field confined between a soft|soft interface with or without a heterogeneous catalyst layer.[26–31]

$$2H_2O \rightarrow H_3O^+ + OH^- \quad K_w \approx 10^{-14} \qquad (1)$$

BPMs typically have a tri-layer structure consisting of an anion-exchange layer (AEL), cation-exchange layer (CEL), and catalyst layer (CL) in the middle (Fig. 1a). The lamination of the alkaline and acidic ionomers gives rise to an equilibrium interfacial electric-potential gradient that is a result of counter-balancing electric and concentration free-energy contributions that ensure equality of the total electrochemical potential across interfaces.[27,32,33] Increasing the electric potential bias/voltage across the BPM results in a thermodynamic driving force for heterolytic WD within the ionic heterojunction. The applied voltage also modulates the electrochemical potential of the ionized WD products once solvated into their respective ionomer phase (Fig. S1 and SI Note S1). The resulting bias-tunable electric field across the BPM makes it ideal for understanding electric-field-dependent reactivity and how exactly bias and the resulting electric-field distribution impacts the rate for WD.

In addition to understanding the interplay of electric fields and catalysis, BPMs can isolate the WD reaction, a foundational chemical reaction that has been under investigation for decades, but is difficult to measure experimentally.[34–36] The mechanisms of WD are paramount in understanding many (bio/electro)chemical systems. WD is important in electrochemical reactions where H_2O is a proton source,[37–39] thermochemical processes such as the water–gas-shift reaction,[40] enzymatic H_2O activation,[41] and other systems. BPMs enable promising reactors for a range of electrochemical applications including H_2O[42] and CO_2 electrolysis,[43–46] CO_2 capture,[47–49] and others, as discussed in previous works.[31] Improved understanding of the fundamental aspects of BPM junctions and the WD reaction could facilitate tailored interfaces and improved performance of these devices and other polarized catalytic interfaces facilitating ion-transfer.

In BPMs the rate of WD is accelerated by heterogeneous catalysts, typically oxides.[26–28,30,42,50–54] The role of the oxide in

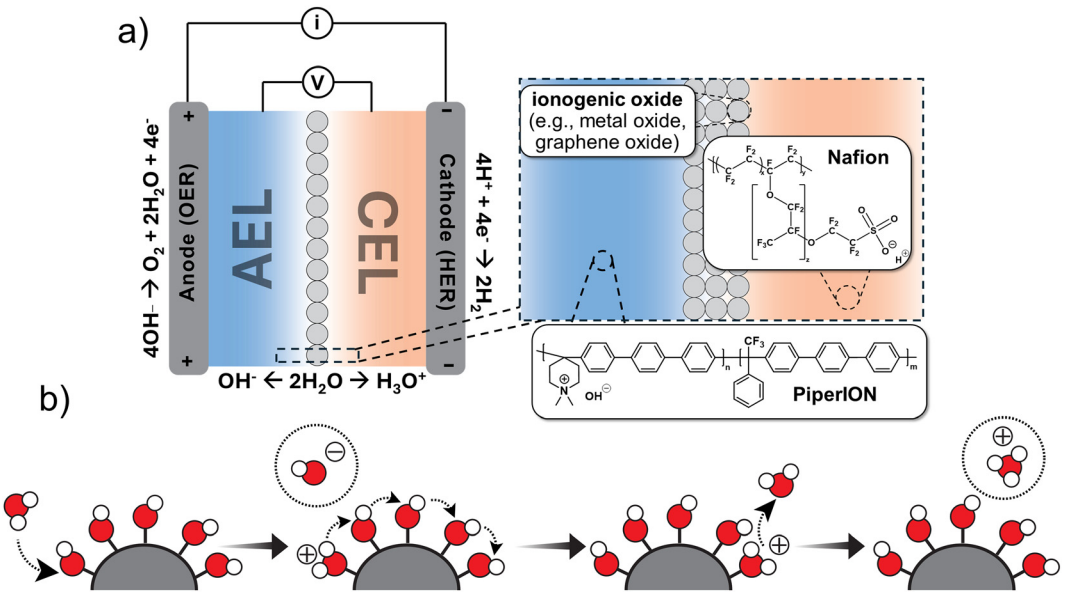

Fig. 1 Overview of BPMs and the role of catalytic WD. (a) The pure-water-fed BPM water-electrolyzer architecture used with the current being applied to the terminal anode and cathode and the membrane potentials being sensed at the CEL and AEL (left). The BPM consists of an oxide CL, Nafion CEL, and Piperion AEL (right). (b) The surface-mediated WD mechanism is thought to proceed *via* a series of proton-transfer steps on the oxide catalyst surface. Dashed arrows represent the movement of H^+.

catalyzing WD has been attributed to a bifunctional effect: (i) the polyprotic oxide surface facilitates WD by a series of elementary proton-transfer steps on terminal S–O(H)$_x$ (x = 0–2) and/or bridging S–O(H)$_y$–S (y = 0–1) oxygen sites (Fig. 1b) and (ii) the electronic and/or dielectric properties of the oxide surface that serve to screen and localize the electric-field distribution through the catalyst-layer (CL) junction.[26–28] Experimental results showed that enthalpic activation barriers to WD on optimal catalysts are nearly insensitive to the overpotential (η_{WD}, the voltage driving force, referenced to equilibrium), which is hypothesized to be due to the potential dependence on rate being driven by electric-field mediated preorganization of H_2O networks lowering only the entropic barrier to WD.[28,29] Alternatively, Bui and others have developed continuum modeling frameworks wherein the Second-Wien effect (operative with and without a catalyst) is invoked to describe an exponential dependence between WD rate and electric field.[32,55–57] Similar results have been found in molecular-dynamics simulations.[58] However, to date there is no direct *experimental* evidence for the Second-Wien effect in BPMs. The BPM junction is complex, particularly in the presence of WD catalysts. The finite-thickness WD CL can both ionically and electronically screen the electrostatic potential gradient through the BPM junction, thus convoluting field effects. Further, the acid/base properties of the oxide are responsive to local fields and concentration gradients. The electric-potential gradient is established as a function of electronic and ionic properties of the buried interlayer at the ionomer heterojunction, thereby making the catalytic and electric-field effects difficult to deconvolute and interrogate.

Here we use a membrane-potential-sensing testbed to show that graphene oxide (GO_x) has a nonlinear bias-dependent rate enhancement for WD, unlike metal-oxide catalysts (*e.g.*, TiO_2). GO_x lowers the enthalpic activation barrier towards WD as a function of η_{WD} in the limit of very large fields, and thus can be used as a high-performance WD catalyst despite deviating from the design principles previously established (namely high *electronic* conductivity).[27,42] A fundamental framework helps rationalize the difference in behavior between GO_x and TiO_2 WD catalysts. The GO_x transport properties are interrogated by constructing CEL|GO_x|CEL and AEL|GO_x|AEL architectures, and the relevant interfaces for WD are explored *via* CL poisoning experiments. These properties are linked to the acid/base properties of the oxide catalyst, which control the electrostatic environment within the heterojunction. While studied here in the context of BPMs, these interfacial phenomena are translatable, and relevant, to other reactions accelerated *via* ion-transit across an electric-potential gradient.

2. Experimental methods

2.1. Porous-transport-electrode preparation

The porous transport electrodes (PTEs) were fabricated *via* air-brushing catalyst inks. Inks were prepared in 20 mL scintillation vials. The anode ink was prepared by adding 0.2 g IrO_2 (Premion, Alpha Aesar), 1 g 18.2 MΩ cm deionized water, 3.4 g IPA, and 0.2 g Versogen PiperION-A5 ionomer suspension (TP85 5 wt%). The cathode ink was prepared identically, except the catalyst was 0.2 g 46.3% Pt/C (TEC10V50E, Tanaka) and the ionomer was Nafion D521 (5 wt%). The inks were subsequently bath sonicated in an ice-bath for at least 1 h, or until fully dispersed.

Following sonication, the inks were airbrushed (Iwata Eclipse HP-CS airbrush) onto their respective porous-transport layers (PTLs) on a hotplate at 60 °C. The anode and cathode PTLs were stainless steel (15FP3, Bekaert Bekipor®) and carbon paper with 5% polytetrafluoroethylene (PTFE) (Toray), respectively, and cut to 30 cm^2 squares. The inks were sprayed onto the PTLs following a serpentine pattern, ensuring the rate of spraying allowed for near-instantaneous drying to avoid over wetting. Over-wetting the PTL allows the catalyst/ionomer to be driven into the bulk of the PTL *via* capillary forces. The final catalyst loading (*e.g.*, IrO_2 or Pt/C) of each electrode was 2.1 ± 0.3 g cm^{-2} measured *via* microbalance. Finally, additional ionomer was sprayed atop the CL until the ionomer loading was 10 to 15% of the total catalyst loading. The catalyst-coated PTLs are denoted PTEs. Before use, the PTEs were die cut into 1.0 cm^2 squares.

2.2. Bipolar-membrane fabrication

BPMs were fabricated using Nafion NR212 and 40 μm Versogen PiperION as the CEL and AEL, respectively. Each membrane was cut into 2 × 2 cm sheets and subsequently pretreated. Nafion membranes were pretreated in ultrapure 18.2 MΩ cm deionized water for at least 24 h before use. The PiperION membranes were treated in a sealed container of 1.0 M KOH solution at least 24 h before use. Immediately before use, the PiperION membranes were transferred to a fresh 1.0 M KOH solution for at least 10 min and finally rinsed for 3 min in an 18.2 MΩ cm deionized water bath prior to assembling the BPM.

The WD CL was applied *via* spray coating from a catalyst-ink suspension. GO_x inks were made by first diluting GO_x (Graphene Supermarket) to 1 wt% in 18.2 MΩ cm deionized water. The GO_x was further diluted to control the GO_x loading, taking between 0.1 to 0.5 g of the 1 wt% ink. 18.2 MΩ cm deionized water was added until the total mass of GO_x ink and water equaled 1 g (this was done to keep the H_2O : IPA ratio consistent). Finally, 0.5 g IPA was added to the ink mixture which was subsequently sonicated for ∼10 min. For the TiO_2 (Alpha-Aesar, Aeroxide P25) inks, TiO_2 was diluted to 0.1 wt% in 18.2 MΩ cm deionized water. The 0.1 wt% solution was then further diluted by adding 0.1 to 0.6 g of the 0.1 wt% solution, which was diluted again to a total mass of 1 g with 18.2 MΩ cm deionized water. Then 0.5 g IPA was added, and the ink was bath sonicated for ∼30 min. We maintained a constant ink volume for both the GO_x and TiO_2 catalysts to allow enough spray passes to promote uniform catalyst-layer formation. Consequently, because TiO_2 requires a lower optimal loading, its ink formulation was prepared at a correspondingly lower concentration. For the SiO_2 poisoning experiments, SiO_2 (US Research Nanomaterials, 99$^+$% 20–30 nm) was first diluted to 0.1 wt% in 18.2 MΩ cm deionized water. Then, 0.2 g of the 0.1 wt% SiO_2 solution was further diluted with 0.8 g 18.2 MΩ cm

deionized water and 0.5 g IPA. For the larger flake size, high surface area graphene oxide (ACS Materials) was used.

An Iwata Eclipse HP-CS airbrush was used to spray coat the CL. The pretreated Nafion 212 coupon was pressed firmly against a clean glass slide, carefully dried with a paper wipe (Kimwipe™), and then the edges were taped down. Well-prepped membranes are absent of air bubbles beneath the membrane, and the taped edges are airtight. The membrane was then placed on a 60 °C hotplate and the CL was airbrushed in short spray bursts allowing instantaneous drying. Following deposition of the CL, the tape was removed, and the membrane was peeled off the slide (without adding excess H_2O). Finally, the BPM was assembled by placing the AEL on a glass slide, slightly dabbing it dry with a paper wipe (but not allowing it to dry entirely), and placing the CEL atop the AEL and pressing it flat with another glass slide. The protocol for fabricating the CEL|CL|CEL and AEL|CL|AEL geometries were identical to the BPM fabrication, except the AEL were heated to 40 °C to avoid AEL degradation. For the catalyst-free cases, the membranes were treated identically to ensure performance was not impacted by the CL deposition process. For the SiO_2 poisoning experiments, an ink (the recipe was identical to that listed above) with 0.2 mg SiO_2 (*e.g.*, 0.2 g of 0.1 wt% SiO_2 ink) airbrushed either directly onto the CEL or onto the AEL side of the CL.

2.3. Electrolyzer fabrication

Electrolyzer measurements were performed in 5-cm^2 hardware from Fuel Cell Technologies, typically masked down to 1 cm^2 with ethylene tetrafluoroethylene (ETFE) gaskets (unless otherwise noted). Serpentine graphite and platinized-titanium flow fields were used at the cathode and anode, respectively. The cell was fabricated *via* first placing a 1.0 cm^2 sintered Ti frit (Baoji Yinggao Metal Materials Co., Ltd, electroplated with ~1 μm Pt) on the anode flow field. ETFE gaskets were added to be 100% the thickness of the frit. Next, the anode PTE was added with additional ETFE gaskets being 85% the thickness of the PTE. The BPM was then placed atop the anode, AEL side down. The cathode and gaskets (85% the thickness of the cathode) were added. Next, another sintered Ti frit, and gaskets equaling the thickness of the frit were added. Finally, the cathode flow field was placed on top of the Ti frit, and the cell was torqued to 5.6 N m. This compressed stack of PTEs and membranes comprised the membrane electrode assembly (MEA). For membrane-potential-sensing measurements, the cell was fabricated identically, with membrane strips extending outside the cell. A Hg|HgO reference electrode was fixed to the AEL and an SCE was fixed to the CEL. Details of the experimental setup are in previous publications.[28] The cell was heated *via* the insertion of resistive heating elements into the anode and cathode endplates, and the cell temperature was monitored *via* a thermocouple inserted into the cathode endplate.

2.4. Electrochemical measurements

All electrochemical measurements were performed using a Biologic SP-300 potentiostat with a 2-A booster channel. When membrane potential sensing was performed, the current-carrying leads P1 and P2 went to the anode and cathode, respectively. The sensing lead S1 went to the Hg|HgO AEL reference electrode, S2 went to the SCE CEL reference electrode, and S3 went to the cathode. 18.2 MΩ cm deionized water was fed to both the anode and cathode at 75 mL min^{-1}. Before each reported measurement, the cell was held at 500 mA cm^{-2} until a nominally steady-state current–voltage response was achieved. For the reported polarization-curves, the current density was stepped from 1000 to 500 mA cm^{-2} in 100 mA cm^{-2} increments, 500 to 50 mA cm^{-2} in 50 mA cm^{-2} increments and finally stepped to 25 mA cm^{-2}. Each current density was held for 30 s. For temperature dependent measurements the maximum current density was 500 mA cm^{-2} and current densities were held for 10 s, except for the first 500 mA cm^{-2} current density, which was held until steady-state was achieved. Galvanostatic electrochemical-impedance-spectroscopy (GEIS) measurements were taken following the polarization curves, with a frequency range of 1 MHz to 1 Hz. Extraneous data points were removed from the Nyquist plots (*e.g.*, typically, occasional noise in the low-frequency regime). The AC current had an amplitude of 10% of the DC current it was superimposed upon. High-frequency-resistance values were taken from the high-frequency regime at which the phase angle approached zero. All electrochemical data reported is at 55 °C unless otherwise noted. For temperature-dependent measurements, the temperature of the water bath fed to the cell, and the cell itself, was varied from 55 to 25 °C in 10 °C increments.

2.5. Zeta potential measurements

pH-dependent zeta-potential measurements were performed using a Malvern Zetasizer Ultra Blue (632.8 nm He–Ne laser) operated in backscatter mode using ZS Xplorer software. All measurements were carried out in folded capillary cells (DTS1070) at 25 °C, with a 120-s temperature equilibration period prior to data acquisition. For each pH condition, measurements were repeated three times, and the reported values represent the average of these replicates. The GO_x and TiO_2, P25 suspensions were prepared at 0.1 wt% in deionized water (using standard values for the refractive index and viscosity of deionized water). For each sample, 2.00 g of suspension was mixed with 4.00 g of 0.050 M KNO_3 to standardize ionic strength, followed by the addition of a small volume of 0.10 M HCl or KOH to adjust the pH. Deionized water was then added to bring the final sample mass to 10.00 g. The final pH values of the prepared suspensions were: GO_x: 2.8, 4.4, 6.1, 8.1, and 12.0; TiO_2: 2.4, 5.5, 9.3, and 12.0. pH measurements were conducted using a calibrated pH meter (Fisher Scientific Accumet AB15). A refractive index of 1.80 (absorption = 0.10) was used for GO_x, and 2.58 (absorption = 0.001) for TiO_2. TiO_2 suspensions were sonicated for 30 min prior to dilution and measurement to ensure the particles remained suspended in solution.

3. Results and discussion

3.1. Polarization behavior of GO_x and TiO_2

Using a membrane-potential-sensing testbed we measured the transmembrane electric potential across the BPM in a zero-gap membrane-electrode-assembly cell (MEA) as a function of

current driving WD. The BPM MEA was operated as a water electrolyzer with proton reduction and hydroxide oxidation at the cathode and anode, respectively (Fig. 1a). Commercially available Versogen PiperION and Nafion ionomers were used as the AEL and CEL, respectively (Fig. 1b). The membrane potentials were measured using reference electrodes ionically connected to each membrane in the device using a membrane-strip testbed (see ref. 28 for details, Fig. S2, and SI Note S2 for discussion on using reference-electrode potentials to obtain electric potential differences). This deionized-water-fed architecture is advantageous as the zero-gap design minimizes impacts of mechanical effects like swelling and delamination that can affect BPM performance. The lack of soluble electrolytes ensures H^+ and OH^- are the only mobile species so that there is no co-ion crossover that otherwise complicates the rigorous interrogation of kinetics and catalytic effects.

The data is presented as a function of η_{WD}, which is taken to be the difference between the measured potential at a given current and the open-circuit potential (the nominal equilibrium electrode-potential difference) measured across the two reference electrodes. The difference in standard potential between the CEL and AEL reference electrodes does not need to be corrected after subtracting the open-circuit potential (*i.e*, the difference in reference potential is constant at the measured potential and open-circuit potential, and therefore cancel).

The current density–voltage (*i*–*V*) response for both the full-cell voltage and η_{WD} are shown in Fig. S3 and Fig. 2a, respectively, for GO_x compared to P25 TiO_2, a prototypical metal-oxide WD catalyst that has been studied previously.[27,28] The curvature of the current–voltage response using the GO_x catalyst is larger than for TiO_2, which has a linear polarization response. The full-cell impedance response is consistent with these results (Fig. S4 and S5). The linear response is consistent with previously reported high-performance BPMs, where metal-oxide catalysts (*e.g.*, TiO_2, SnO_2, *etc*...) yield nearly linear bias-dependent rates at their optimal loading.[28,42] The nonlinear kinetic response of the GO_x BPM parallels that of electrocatalytic reactions, wherein changes in electrode potential away from equilibrium produces an exponential rate dependence. The exponential dependence is thought to be due to changes in the free-energy of the reaction with voltage using a transition-state-theory framework.

The GO_x WD catalyst exhibits good performance,[42] with WD overpotentials of ~190 mV at 1 A cm^{-2}. For reference, an optimized homemade SnO_2 WD catalyst reported achieve overpotentials of ~100 mV at 1 A cm^{-2} and 55 °C, which is the best performance to date.[42] The performance shown here is better than the performance achieved previously with GO_x-based catalysts (~250 mV at 1.0 A cm^{-2}).[30] The different operative modes of GO_x relative to TiO_2 and other previously reported metal oxides suggests the local electrostatic environment around an ion-transfer catalyst can directly influence catalyst design principles, where catalysts with larger field-enhancements may be preferrable at more polarized interfaces.

Here, the difference between the GO_x and TiO_2 bias-dependent WD rate indicates an underlying fundamental mechanistic difference. Identifying the chemistry and physics that give rise to these differing bias-dependent behaviors are important to elucidate the mechanisms and drivers behind WD, along with the complexities associated with the formation and polarization of catalyzed ionic heterojunctions.

3.2. Loading dependence of the GO_x catalyst layer

The loading-dependence WD rate was compared between the GO_x and P25 TiO_2 catalyst. With P25 TiO_2, the WD kinetics depend strongly on the CL mass loading (Fig. 2b).[27,28] It was previously argued that as the loading is increased towards the optimum, the larger number of active sites increases the reaction rate (as is typical in heterogeneous catalysis), while at loadings larger than the maximum, the decrease in WD activity is due to a decreasing electric-field magnitude at the catalyst surface.[59]

Unlike P25 TiO_2, the WD kinetics for the GO_x catalyst is largely independent of mass loading, with only minor increases in overpotentials at very high loadings. This differs from

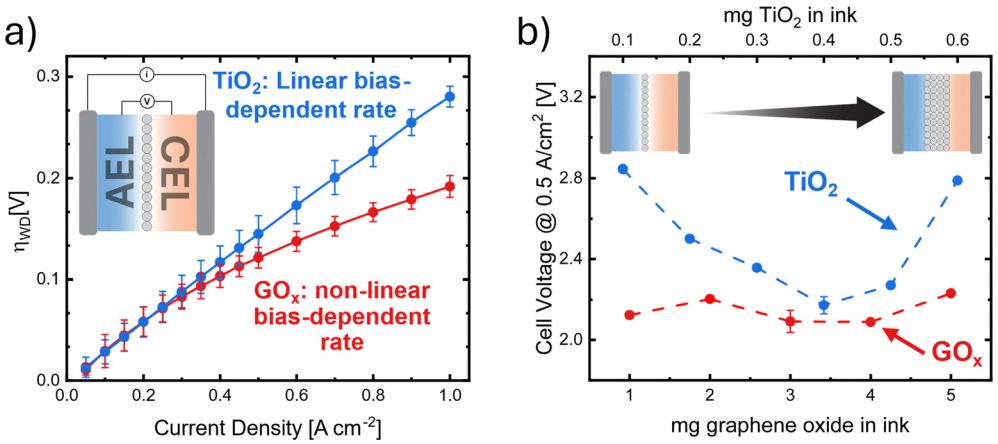

Fig. 2 Current–voltage response and loading dependence of TiO_2 and GO_x BPMs. (a) Full-cell potential *vs.* current density of the BPM water electrolyzers. (b) Dependence of WD-catalyst loading on polarization response. All measurements recorded at 55 °C.

previous reports of the apparent loading-dependent activity for GO_x catalysts, wherein those may be convoluted with mechanical artifacts associated with measurement in an H-cell compared to the MEA used herein where the sample is under static compression.[30,54]

Within our previous framework for understanding WD catalysts,[27,28] the independence of η_{WD} on the loading suggests that both the number of WD catalyst active sites and relative electric-field magnitudes are constant. This result is consistent with (i) WD for GO_x being operable at only the interface with either both or one of the ionomer junctions, and not in the bulk of the added GO_x layer, and (ii) facile ion transport through the GO_x layer. Previous studies have also noted that catalysts with high electronic conductivity tend to have less-pronounced loading dependences.[27,42] Materials of high electronic conductivity (*e.g.*, Pt (metallic) or IrO_2 (semi-metallic)) should screen the electric field in the solid, which increases the electric field in the interparticle gaps or boundaries of the bipolar junction.

GO_x is nominally an electronic insulator and therefore electric-field screening across the bipolar junction *via* electronic polarization is unlikely. These new data demonstrate that the rate of WD is seemingly unchanged as a function of GO_x loading, something that previously reported physical pictures cannot explain. Fig. S6 shows two different GO_x CLs at the same loading; our baseline Graphene Supermarket GO_x and a high-surface-area GO_x (ACS Materials). We observe that despite the markedly different average GO_x flake size, the WD catalysts exhibit similar performance. Because of the insensitivity of BPM performance to GO_x loading and morphology, fabricating these BPMs at scale may be more reproducible and straightforward than with the oxide particles.

3.3. Proton and hydroxide conductivity through GO_x BPMs

The minimal dependence of WD rate on GO_x loading led us to next interrogate the spatial distribution of the WD reaction through the thickness of the BPM junction. We hypothesized that the reactive domain within the heterojunction is likely defined by both the catalyst acid/base and electronic properties, which can both screen the electric potential within the heterojunction. Zeta-potential measurements show that GO_x surface oxygen sites are deprotonated across a broad range of pH values, and only change minimally with pH (Fig. S7). Similar results were reported for GO_x by Lv *et al.*[60] This result is attributed to the acidic carboxylate-species on the GO_x surface. Thus, it seems that the pH gradient through the BPM with a GO_x CL exists predominantly at the AEL|GO_x interface, resulting in a large electric-potential gradient at that interface. Similarly, if the GO_x CL is acidic, it should be resistive to OH^- transport, thereby resulting in WD being localized at the GO_x|AEL interface, circumventing any OH^- flux through the GO_x. The H^+ concentration and conductivity in the acidic GO_x CL thus would screen the electric field and focus it at the AEL|GO_x interface. This physical picture is similar to the results of continuum simulations.[30] In contrast, TiO_2 has many protonatable sites in the entire pH range tested. Thus, for TiO_2, the pH gradient would be less localized and correspondingly have a less localized electric-potential gradient in the BPM.

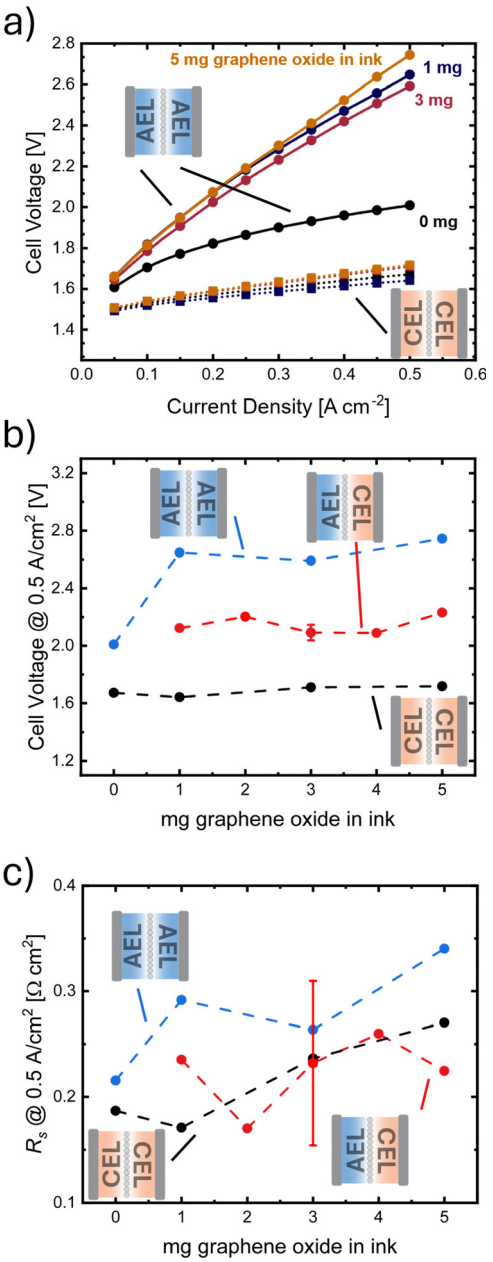

Fig. 3 The impact of GO_x WD catalysts loading in BPMs (a) *i*–*V* curves for the AEL|GO_x|AEL and CEL|GO_x|CEL devices with various GO_x loadings. (b) The cell voltage of CEL, AEL, and BPM devices as a function of the interlayer GO_x loading. (c) The high-frequency resistance increases only slightly as a function of GO_x loading for all architectures.

To test the above hypothesis, we measured the resistance to transport of OH^- *versus* H^+ through the GO_x interlayer. We fabricated a proton-exchange-membrane water electrolyzer (PEMWE) with a CEL|GO_x|CEL geometry and an anion-exchange-membrane water electrolyzer (AEMWE) with a AEL|GO_x|AEL geometry. Polarization curves and electrochemical impedance spectroscopy (EIS) were measured on both devices as a function of GO_x loading (and therefore CL thickness) as shown in Fig. 3.

The PEMWE polarization curves, along with the high-frequency resistance (R_s) extracted from impedance analysis, changed minimally as GO_x was added and as a function of thickness (Fig. 3a–c). In contrast, the cell potential increased substantially for the AEMWE upon addition of the GO_x interlayer. However, within the limit of experimental reproducibility, AEMWE device performance was relatively insensitive to additional increases in the GO_x loading (Fig. 3a and b), which is indicative of dominant interfacial ionic resistance, as opposed to a bulk resistance for ion transport in the GO_x layer. These results are consistent with the hypothesis that the high-acidity of the GO_x surface is conductive to protons but not hydroxide. This data also highlights the differences compared to TiO_2 WD catalysts, which conduct both OH^- and H^+ in a similar experiment (*i.e.*, both demonstrate relative insensitivity to cell architecture).[27]

We explain these findings as follows. In the case of the AEL|GO_x|AEL system, OH^- are excluded from the acidic GO_x layer (*via* Donnan effects[61]) and thus the overall system becomes a type of tripolar device where one AEL| GO_x interface performs WD and the other performs $H^+ + OH^-$ recombination to drive ionic current through the system; protonic current is driven through the acidic GO_x layer (Fig. 4a). The negative charge density within the GO_x layer interfacing with the

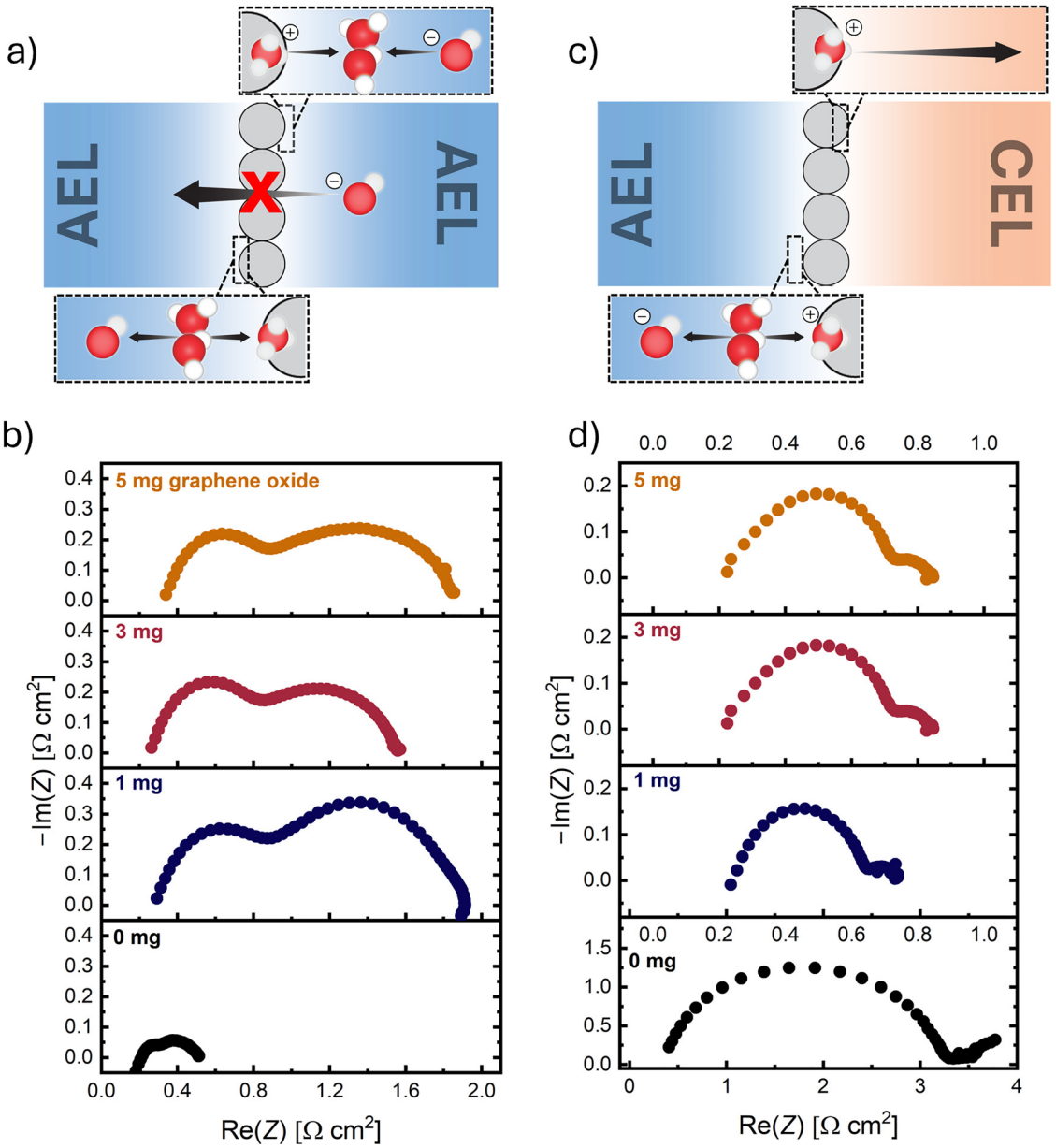

Fig. 4 Proposed mechanism of ion-transport processes in the AEL|GO_x|AEL and BPM systems and the respective loading-dependent impedance responses. (a) Hypothesized mechanism to pass ionic current through the AEL|GO_x|AEL device. (b) Nyquist plots of the AEL|GO_x|AEL devices with differing amounts of GO_x loading at 500 mA cm^{-2}. (c) WD enables ionic current through the BPM. (d) Nyquist plots of the BPM water electrolyzer with differing amounts of GO_x loading at 500 mA cm^{-2}.

cationic charge at the AEL layers provides electrostatic-potential gradients to drive the interfacial WD reactivity, but introduces the interfacial resistances found experimentally. This physical picture is also consistent with the relatively small changes in R_s for the AEL|GO_x|AEL device as a function of GO_x layer loading because protonic current is easily driven through the GO_x layer. This interpretation is also supported in the EIS spectra (Fig. 4b). For the bare AEL|AEL system we find two semicircles in the Nyquist plot corresponding to the anodic and cathodic charge-transfer resistances. In the AEL|GO_x|AEL systems we find two much-larger semicircles. The charge-transfer resistance from the electrodes should be independent of the presence of the CL. We conclude that the growth of these semicircles is not due to changes in the electrode processes but arise from the WD and H^+/OH^- recombination reactions at the respective AEL|GO_x|AEL interfaces. The impedance across the BPM is largely insensitive to GO_x loading, and thus WD occurs locally at the AEL|GO_x interface, while H^+ conduction through the GO_x layer is sufficiently fast (Fig. 4c and d). Together, these results demonstrate that given the high performance of the GO_x WD CLs in the BPM, protons are the charge carriers in the GO_x catalyst.

To test the hypothesis that the GO_x|AEL interface is responsible for facile WD, we intentionally poisoned either the CEL or AEL with SiO_2 nanoparticles that are known to be very poor catalysts for WD.[27] Briefly, 0.2 mg of SiO_2 was sprayed directly onto the AEL or CEL before fabricating the GO_x CL. We find that poisoning the CEL interface only minimally impacts the WD polarization curve, whereas poisoning the AEL interface increases the cell voltage by >200 mV relative to the pristine GO_x BPMs (Fig. 5). The impedance response exhibits substantially larger charge-transfer resistances in the high-frequency regime when the SiO_2 layer is on the AEL relative to the CEL (Fig. S8), consistent with the polarization curves. This data is a strong indication that the interface responsible for WD in GO_x BPMs is solely the AEL|GO_x interface.

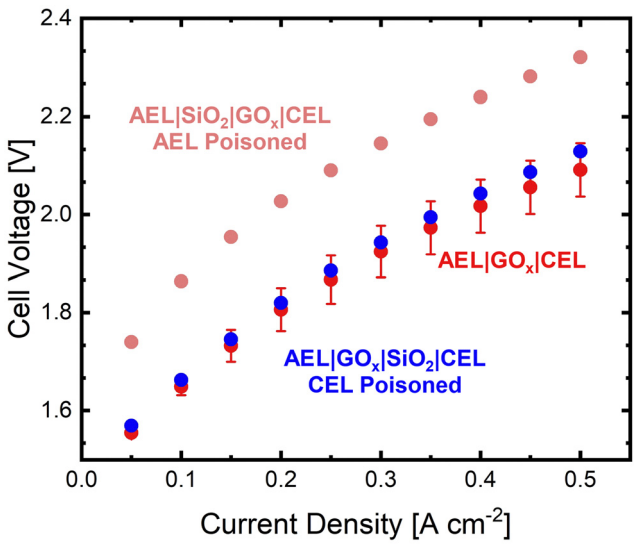

Fig. 5 Polarization curves of GO_x BPMs poisoned with SiO_2 on either the CEL or AEL. SiO_2 sprayed onto the AEL substantially reduces performance, whereas SiO_2 sprayed onto CEL only minimally impacts performance.

3.4. Arrhenius analysis of polarization-dependent kinetics

To explore the *i–V* behavior further, polarization curves were measured at 25, 35, 45, and 55 °C and an Arrhenius analysis was performed (Fig. 6a and b). The Arrhenius equation can be written as $i = Ae^{-\frac{E_a}{RT}}$. Here A is the Arrhenius preexponential factor in A cm^{-2}, typically associated with the rate of collisions *via* transition-state theory and related to the entropy of activation (per the Eyring–Polanyi equation), E_a is the apparent enthalpic activation barrier, R is the universal gas constant, and T is absolute temperature. Plotting the ln(i) *versus* 1000 T^{-1} a typical Arrhenius response is realized with a quasi-temperature-independent pre-exponential factor at potentials ranging from η_{WD} = 20–120 mV (Fig. 6c). The polarization curves were measured under galvanostatic operation, thus interpolation *via* cubic splines was used to extract current densities at constant η_{WD}. In the case of TiO_2, A scales approximately linearly with applied η_{WD} with fit values ranging from $\sim 3 \times 10^2$ to 4×10^3 A cm^{-2} across the potential range of interest, which are in decent agreement with both Chen and Rodellar (Fig. 6d).[28,29] Similarly, we find E_a to be ~23 to 25 kJ mol^{-1} and is independent of η_{WD}, again in agreement with previous work (Fig. 6e). This is in contrast to TiO_2, where, within experimental error, A is on the order of 10^5 A cm^{-2} and only slightly decreases with η_{WD} (the large error is likely associated with the data extrapolation used to obtain A) (Fig. 6d). Furthermore, E_a decreases roughly linearly as a function of η_{WD} from ~40 to ~32 kJ mol^{-1} for 20 to 120 mV of overpotential, respectively (Fig. 6e). The bias-dependence of E_a was fit using a linear-free energy relationship (eqn (2)).

$$E_a(\eta_{WD}) = E_a^0 - \alpha F \eta_{WDw} \quad (2)$$

here E_a^0 is the apparent thermal activation barrier at zero overpotential, F is Faraday's constant, and α is a fitting coefficient describing the sensitivity of the activation energy to overpotential (*i.e.*, a proton-transfer coefficient). For GO_x, the activation barrier is sensitive to the applied bias with $\alpha = 0.68 \pm 0.06$, while for TiO_2 there is minimal relation between η_{WD} and E_a and $\alpha = -0.08 \pm 0.02$ (notably the negative α value indicates a slight increase in E_a with increasing η_{WD}, perhaps an artifact of the measurement). Due to the surprisingly large α value for GO_x, the Arrhenius data was also fit with a constant prefactor, to preclude the possibility of systematic error in the fit (Fig. 6f), resulting in $\alpha = 0.48 \pm 0.02$.

3.5. A framework for GO_x water dissociation

To develop a framework towards understanding WD with different catalysts, we first dissect the driving forces for WD. As defined previously, our measured overpotential for WD is η_{WD}, which is related to the total free-energy change associated with the overall process of dissociating water and separating the incipient ions. The local driving force for a single WD event, however, is heterogeneous across the BPM junction, and

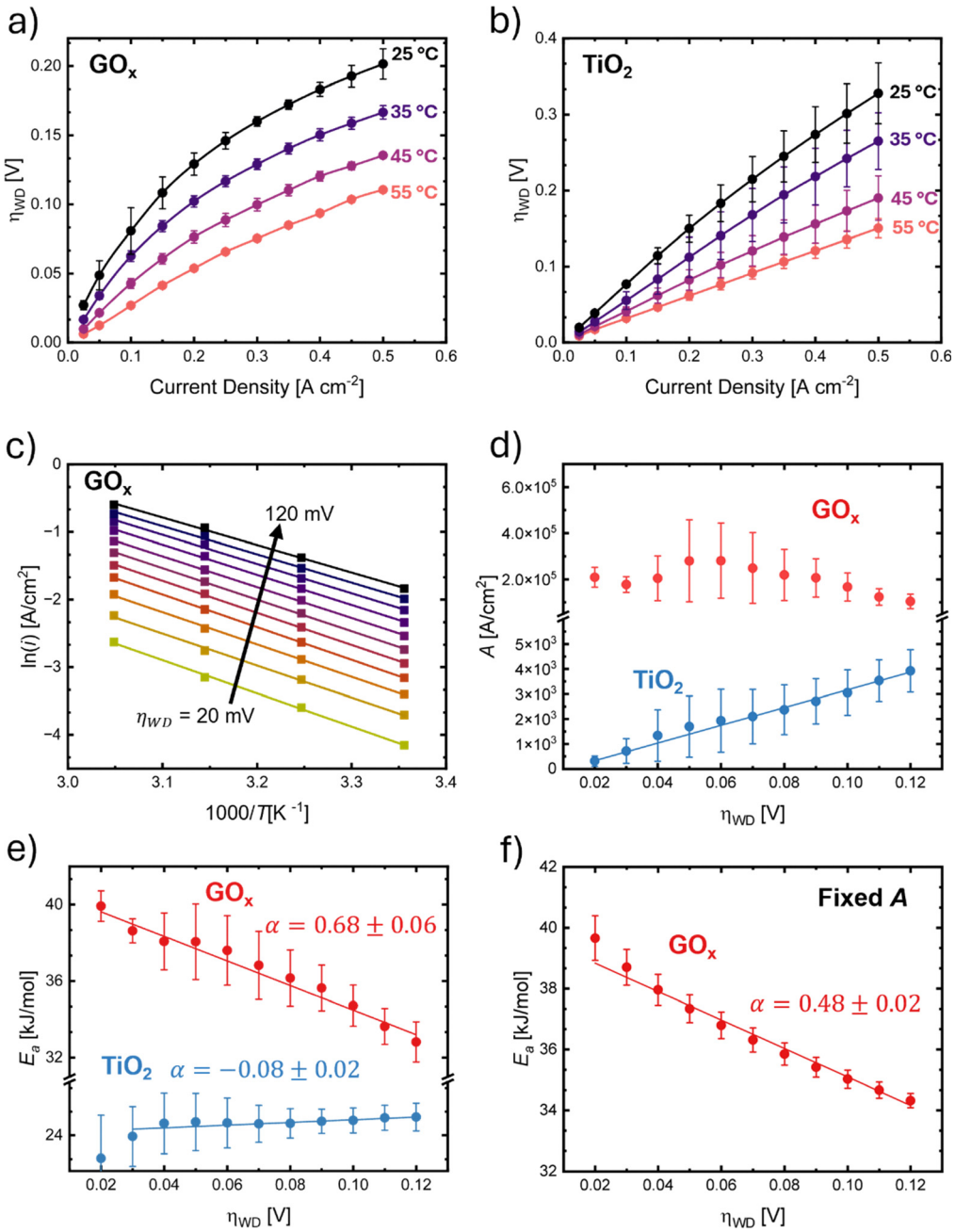

Fig. 6 Temperature-dependent behavior of GO_x and TiO_2 BPMs. Temperature-dependent i–V curves for the (a) GO_x and (b) TiO_2 BPMs. (c) A representative Arrhenius plot for a GO_x BPM. (d) Potential dependence of the Arrhenius preexponential factor, A. (e) Potential dependence of the thermal activation barrier, E_a. TiO_2 exhibits an E_a independent of η_{WD} whereas GO_x shows a linear correlation with η_{WD}. The α value is the sensitivity of E_a to η_{WD} per the linear-free-energy relationship in eqn (2). (f) E_a as a function of η_{WD} when the GO_x Arrhenius fits were performed with a fixed A. The fixed A value was selected to be the average A recovered from panel (d) (201 874 A cm^{-2}).

in some cases, will be far less than η_{WD}. A better understanding of these local driving forces is required.

To understand these driving forces, it is useful to first consider traditional Butler–Volmer kinetics. Assuming large overpotentials, and no mass-transfer limitations, Butler–Volmer can be reduced to the Tafel expression for one half reaction:

$$i = i_0 e^{-\frac{\alpha_{BV} F \eta}{RT}} \quad (3)$$

where i_0 is the exchange current density, α_{BV} is the phenomenological transfer coefficient (notably, not the symmetry factor which is a theoretical value reporting on the shape of the energy barrier of an elementary single-electron transfer process). The driving force for charge transfer is proportional to $\alpha_{BV}\eta$ where α_{BV} is typically between 0 and 1. Physically, α_{BV} can be thought to represent the fraction of overpotential that contributes to reducing the activation energy. When α_{BV} is zero, the applied voltage is independent of η, and, when α_{BV} is one, the apparent

barrier decreases by an amount equal to the applied overvoltage. In traditional half-cell measurements, however, the electric-potential drop occurs directly at the electrode|electrolyte interface, typically within 0.1 to 10 nm of the surface.[62] Thus, defining a single overpotential scaled by a fitted prefactor is reasonable to represent the average of an ensemble of nonidentical sites.

BPMs have a more-complex potential drop that occurs across the heterojunction. To capture these complexities, we consider the local driving force at site i as $\eta^*_{i_{WD}}$, which is the deviation of the local overpotential of an active site from the local equilibrium potential. The term $\eta^*_{i_{WD}}$ is a function of the local electric-potential difference relative to the local equilibrium electric-potential difference ($\Delta\phi^\star$ and $\Delta\phi^*_{eq}$, respectively) and the deviation in activity of H^+ and OH^- from equilibrium. From this, a generic one-dimensional rate expression for WD may be written, where the rate constants are functions of $\eta^*_{i_{WD}}$ and $\Delta\phi^*_{eq}$ (eqn (4)). There are also other parameters not considered explicitly here due to the simplified rate expression chosen, which could possibly impact the observable rates.

$$i_{WD} = F\int_0^L \left[k_{WD}\left(\eta_i^*(x), \Delta\phi^*_{eq}(x)\right)\cdot a_{H_2O}(x) - k_{RC}\left(\eta_i^*(x), \Delta\phi^*_{eq}(x)\right)\cdot a_{H^+}(x)\cdot a_{OH^-}(x)\right]dx \quad (4)$$

The rate constants for WD and H^+/OH^- recombination are k_{WD} and k_{RC}, respectively, a_i is the activity of species i, x is position within the bipolar junction, and L is the total thickness of the bipolar junction. Below, the impact of each variable is considered in turn.

First, consider the role of $\Delta\phi^*_{eq}$. The electric field through the heterojunction is established *via* excess charges in the ionomer phases and can be localized *via* ionic or electronic screening. The equilibrium electric-potential gradient at a site dictates the interfacial solvent structure. A larger electric field at the catalyst surface induces increased solvent ordering and can also increase the strength of the hydrogen-bond network.[63] In the context of transition-state theory, $\Delta\phi^*_{eq}$ can impact the prefactor, A. For example, a reduction in interfacial solvent entropy can increase the apparent prefactor if the solvent organization prefers a low-entropy transition state. $\Delta\phi^*_{eq}$ is also linked to the H^+ (or OH^-) activity gradient through the heterojunction. As both the CEL and GO_x have acidic character, most of the electric potential is anticipated to drop at the GO_x|AEL interface, where the largest a_{H^+} gradient exists (as discussed above). This would give rise to a large local electric field at that interface, and therefore, we hypothesize, a large prefactor. Indeed, the Arrhenius analysis determined an A value ($\sim 10^5$ A cm^{-2}) substantially larger than calculated for TiO_2 as well as those reported elsewhere.[28,29,42] TiO_2 is less acidic and its surface charge is highly pH dependent (Fig. S7). Thus, as a function of position in the heterojunction, variable protonation states exist on TiO_2 along with local interparticle potential drops (as charge polarizes on the particle in the field). Hence, the local electric fields would be notably smaller than the well-screened case of GO_x, resulting in the smaller prefactor ($<10^3$ A cm^{-2}). This role of *ionic* charge in screening the electric field to drive WD has largely been overlooked in previous work, but appears critical to understanding WD kinetics here.

Common kinetic formalisms often consider the deviation of the interfacial potential away from equilibrium but not the magnitude of the equilibrium fields. As recently discussed in the context of the hydrogen-evolution-reaction (HER) kinetics (where WD coupled to electron transfer is the common rate-determining step (RDS)) and CO_2 reduction, the absolute magnitude of the interfacial fields can effect reaction kinetics and solvent/adsorbate free energies.[15,64–67] Koper and coworkers have concluded that the rate-limiting Volmer step ($H_2O + e^- \rightarrow H_{ads} + OH^-$) is slow in alkaline media due to large overpotentials associated with the rigid solvation environment that must reorganize to solvate the incipient OH^- ion.[68] Electrified interface, even if at equilibrium, are thus highly complex, as the local microenvironment and free-energy of all species is dictated *via* the local chemical and electrostatic environments. To capture these complexities, it is necessary that interfacial fields both at, and far from, equilibrium are considered.

We now consider the local electric-potential gradients when the system is biased. If increased driving force is supplied across the BPM, there is a corresponding increase in $\Delta\phi^\star$ away from $\Delta\phi^*_{eq}$. If the interfacial solvent entropy is responsive to $\Delta\phi^\star$, an increase in A could be expected with increased electric-potential gradients. This is the behavior observed here for TiO_2 (Fig. 6d), where increasing η_{WD} corresponds with a linearly increasing A and is consistent with the physical picture of field-driven interfacial solvent ordering. For GO_x, A is seemingly independent of transmembrane potential, even though our above results suggest a larger fraction of the excess electric potential drop is occurring at the WD-active AEL|GO_x interface. This is rationalized by assuming that given a sufficiently large interfacial field, there is saturation of the interfacial solvent ordering as the interface structure and A might become quasi-electric-field-independent. Recent *ab-initio* molecular-dynamics simulations calculated a saturation of bulk H_2O ordering in the presence of large fields, supporting this hypothesis.[69]

The local electrostatics and driving forces can also impact E_a, as observed here with GO_x. The sensitivity of E_a is defined *via* α in eqn (2). Previous works have associated α with the fraction of the electric-potential drop available for a single H^+ transfer event.[28] The O–H bond length in H_2O is $\sim$0.1 nm and hydrogen bonds are $\sim$0.2 nm, thus the H^+ transfer distance is $\sim$0.1 nm.[28,34] From this physical picture, if α is $\sim$0.68, the total electric-potential drop occurs over $<$0.2 nm. It is unlikely that the electric-potential drop is sufficiently confined to support the α value calculated for GO_x if the impact of the overpotential

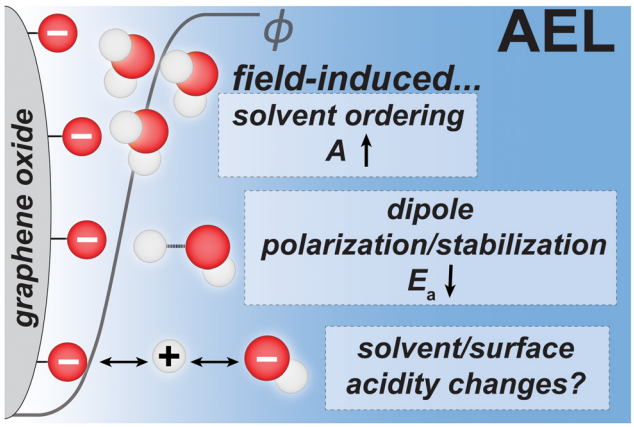

Fig. 7 The role of electric fields in facilitating ion transfer. Electric fields at the catalyst surface can induce changes in interfacial solvent ordering, local molecular dipoles in the reactant, product, and transition state, and local acid–base chemistry of both the solvent and catalyst.

is only related to the fraction of overpotential across a single H^+ transfer. Below, other possibilities that may act in tandem and ultimately give rise to the experimental results (Fig. 7) are explored.

We hypothesize that the H^+ transfer enthalpic barrier can be reduced two ways: (i) field-driven stabilization of the H^+ transfer, and (ii) field-induced changes in ground-state interfacial solvent/catalyst acid–base properties. In the case of the former, the H^+ is transiting down an electric-potential gradient during WD. The larger this gradient, the greater stabilization, and thereby the lower E_a becomes. This is similar to the Second-Wien effect.[24,32] This interpretation necessitates a "product-like" transition state, because the H^+ needs to have appreciably moved in the field for the barrier to have its energy augmented electrostatically. This is consistent with the relatively large α parameter recovered, where larger α corresponds with a more product-like transition state. One can also relate this view to Hammond's postulate and related Bell–Evans–Polanyi scaling relationships between free-energy change and activation barrier.[70] In the case of the latter, the electric field can act upon the dipole of interfacial H_2O and surface-dipole of the catalyst while in the reactant state; electronic polarization could change the relative stability of protons on the H_2O or GO_x. These additional effects could give rise to the large α values observed here, that are seemingly non-physical if only considering transition-state stabilization.

For TiO_2, E_a is nominally independent of η_{WD} ($\alpha \approx 0$) and increased voltage increases A. This is a signature of an early transition-state. The excess field might predominantly change the structure/entropy of the interfacial H_2O with larger fields leading to lower-entropy reactant state and thus a lower entropic barrier to the transition state – without affecting the enthalpic barrier.

Fig. 6e shows that E_a for GO_x is much larger than for TiO_2, in particular at low overpotentials (for $\eta_{WD} \rightarrow 0$, $\sim$40 *vs.* $\sim$24 kJ mol^{-1}). Perhaps, E_a is dictated *via* the acid/base properties of the oxide surface and the relative local pH set by each reactive interface. For example, the rate constants for protonation of amino acids is higher when the pK_a is greater than the local pH, and *vice versa* for deprotonation.[71] In the case of the acidic GO_x, the large E_a might be due to the acidic surface having less-favorable H^+ binding sites. An amphoteric surface, like TiO_2, may have sites favorable for both H^+ binding and H^+ release. Future studies regarding the role of acid/base properties in defining the overall magnitude in E_a would be valuable. An ideal WD catalyst would simultaneously have low E_a at small overpotentials, whilst having large field-effects. Perhaps, materials that have both strongly acidic sites to set the large interfacial Donnan potential, and near-neutral sites for facile H^+ adsorption/desorption, would be idealized material.

3.6. A molecular picture of water dissociation

From these results we hypothesize a mechanism for WD on GO_x. The acidic GO_x surface is far from its PZC at the GO_x|AEL interface, and thus we expect the reaction to be initiated *via* a surface-bound oxygen-anion accepting a H^+ from an interfacial H_2O molecule with concerted solvation of OH^- into the local solvent and subsequently the AEL (eqn (5)). Charge separation then occurs *via* the translocation of the H^+ *via* Grothuss hopping along the GO_x surface, perhaps mediated by surface water (see eqn (6) where * is used to distinguish between two GO_x sites). Subsequent solvation of the H^+ into the CEL (eqn (7)) completes the WD process. Release of the H^+ into the CEL is likely more facile than the initial protonation step (eqn (5)), because of the acidity of the GO_x surface. This interpretation is supported by the CEL|GO_x|CEL experiments where GO_x must also transfer protons into the CEL and where the PEMWE voltage was insensitive to the inclusion of GO_x (Fig. 3b); H^+ release into the CEL must be facile. The rate-determining step in WD on GO_x is thus likely the protonation of the GO_x at the AEL interface (eqn (5)).

$$GO\text{–}O^- + H_2O \rightarrow GO\text{–}OH + OH^-_{aq,AEL} \quad (5)$$

$$[GO\text{–}OH + {}^*GO\text{–}O^- \rightarrow GO\text{–}O^- + {}^*GO\text{–}OH] \quad (6)$$

$${}^*GO\text{–}OH + H_2O \rightarrow H_3O^+_{aq,CEL} + {}^*GO\text{–}O^- \quad (7)$$

Previous works have hypothesized the WD is most facile where the oxide is closest to its PZC.[26,29] Our data suggests that WD proceeds where there is the largest local driving force for WD (*e.g.*, $\eta^*_{i_{WD}}$). At equilibrium, the local electric-potential gradients are largest where there is the largest pH gradient. For GO_x, most of this exists at the AEL|GO_x interface. For TiO_2 (and most metal oxides), there are likely pH gradients extending throughout the heterojunction, as the oxide protonation state has a roughly linear-dependence on the local pH. This would likely result in the WD driving forces being less localized. This, in part, is likely why there exists complex loading-dependences that depend on the type of catalyst, where the number of active sites and local driving forces are competing effects.

Each of the steps indicated in the proposed molecular WD mechanism (eqn (5)–(7)), in principle, can have their activation

barrier reduced in the presence of an electric field. However, this differs from assumptions in modeling studies by others.[31,32,56,57] Legacy models use the Second-Wien Effect as the operative mechanism for electric-field enhanced WD. However, the field enhancements were only operative for reactions that generate net charge. This is reasonable in the limit of bulk solvent ionization where net-charge generation is inherent to heterolytic bond cleavage. However, in the mechanism proposed here, net charge is not generated in the RDS. Instead, charge is transiting an electric-potential gradient and being abstracted by the catalyst surface. The Second-Wien Effect expressions for bulk solvents may thus not capture the complete physical picture.

4. Conclusion

Through the study of the WD reaction in BPMs, this work provides a broader understanding of the rate-controlling physical and chemical elements of ion-transfer under strong electric fields. It is shown how interfacial electric fields can change both the enthalpic and entropic transition-state barriers. For amphoteric metal oxides like TiO_2, smaller local electric fields seemingly induce solvent interfacial ordering that change entropic barriers. Highly acidic GO_x catalysts effectively localize a much larger electric field to the AEL|CL interface, which impacts enthalpic barriers probably due to field-induced changes in the ground/transition-state dipole moments of both solvent and catalytic active sites. For GO_x, $>50\%$ of the applied driving force went towards reducing the enthalpic transition state barrier (from $\sim$40 to 33 kJ mol^{-1} with 120 mV applied overpotential), whereas for TiO_2 the barrier was nominally insensitive to driving force. The opposite was true for the entropic barrier, where for TiO_2 the driving force reduced the barrier, and for GO_x the barrier was insensitive to this driving force. Notably, however, the large equilibrium interfacial fields for GO_x results in a very large (but voltage-independent) pre-factor. This GO_x catalyst has performance on par with the best commercially available WD catalysts, despite this entirely different operative mechanism. We emphasize the importance of considering the ionic character of the oxide catalyst when considering the physics of ionic heterojunctions broadly. The role of the ionic character is shown through a series of membrane architectures (*e.g.*, CEL|CL|CEL and AEL|CL|AEL), CL poisoning experiments, and loading-dependence studies. These studies show the ionic character of the oxide dictates both kinetic and transport processes through the junction. This work sets the stage for the informed design of catalysts that can leverage both ionic and electronic properties, and their interactions with interfacial electric fields, to accelerate field-enhanced interfacial reactivity across many systems.

Author contributions

TNS, JCB, SWB, and AZW conceived the study. TNS performed all electrochemistry experiments. YW assisted with zeta potential measurements. SH assisted with the membrane potential sensing experiments. TNS performed all data analysis and wrote the original draft of the manuscript. All authors participated in providing intellectual insight, editing, and finalizing the manuscript. JCB, SWB, and AZW provided project oversight.

Conflicts of interest

SWB has patents on bipolar membrane catalysis and fabrication and is an advisor to a startup company commercializing this technology.

Data availability

The data supporting this article are included in the main article and supplementary information. Additional raw data supporting the findings of this manuscript are available upon reasonable request from the corresponding author.

Supplementary information (SI) is available. See DOI: https://doi.org/10.1039/d5ey00364d.

Acknowledgements

The authors are thankful for insightful discussions with members in the Berkeley Lab Energy Conversion Group, and University of California, Berkeley, Boettcher Group. This work was supported by US Department of Energy, Office of Science through the Center for Ion Management in Electrochemical Systems and Center for Ionomer Based Water Electrolysis both under contract DE-AC02-05CH11231. T.N.S. acknowledges support from the National Science Foundation Graduate Research Fellowship (NSFGRFP) under Grant No. DGE 2146752.

References

1 F. Che, J. T. Gray, S. Ha, N. Kruse, S. L. Scott and J.-S. McEwen, *ACS Catal.*, 2018, **8**, 5153–5174.
2 C. F. Gorin, E. S. Beh, Q. M. Bui, G. R. Dick and M. W. Kanan, *J. Am. Chem. Soc.*, 2013, **135**, 11257–11265.
3 C. F. Gorin, E. S. Beh and M. W. Kanan, *J. Am. Chem. Soc.*, 2012, **134**, 186–189.
4 D. M. Harraz, K. M. Lodaya, B. Y. Tang and Y. Surendranath, *Science*, 2025, **388**, eads7913.
5 X. Huang, C. Tang, J. Li, L. C. Chen, J. Zheng, P. Zhang, J. Le, R. Li, X. Li, J. Liu, Y. Yang, J. Shi, Z. Chen, M. Bai, H. L. Zhang, H. Xia, J. Cheng, Z. Q. Tian and W. Hong, *Sci. Adv.*, 2019, **5**, eaaw3072.
6 J. Ryu and Y. Surendranath, *J. Am. Chem. Soc.*, 2019, **141**, 15524–15531.
7 C. G. Vayenas, S. Bebelis and S. Ladas, *Nature*, 1990, **343**, 625–627.
8 T. S. Wesley, Y. Roman-Leshkov and Y. Surendranath, *ACS Cent. Sci.*, 2021, **7**, 1045–1055.
9 K. S. Westendorff, M. J. Hulsey, T. S. Wesley, Y. Roman-Leshkov and Y. Surendranath, *Science*, 2024, **383**, 757–763.

10 Z. Zhao, R. Bababrik, W. Xue, Y. Li, N. M. Briggs, D.-T. Nguyen, U. Nguyen, S. P. Crossley, S. Wang, B. Wang and D. E. Resasco, *Nat. Catal.*, 2019, **2**, 431–436.
11 T. S. Wesley, M. J. Hulsey, K. S. Westendorff, N. B. Lewis, E. J. Crumlin, Y. Roman-Leshkov and Y. Surendranath, *Chem. Sci.*, 2023, **14**, 7154–7160.
12 S. D. Fried, S. Bagchi and S. G. Boxer, *Science*, 2014, **346**, 1510–1514.
13 S. D. Fried and S. G. Boxer, *Annu. Rev. Biochem.*, 2017, **86**, 387–415.
14 J. Resasco, L. D. Chen, E. Clark, C. Tsai, C. Hahn, T. F. Jaramillo, K. Chan and A. T. Bell, *J. Am. Chem. Soc.*, 2017, **139**, 11277–11287.
15 L. D. Chen, M. Urushihara, K. Chan and J. K. Nørskov, *ACS Catal.*, 2016, **6**, 7133–7139.
16 E. W. Lees, J. C. Bui, O. Romiluyi, A. T. Bell and A. Z. Weber, *Nat. Chem. Eng.*, 2024, **1**, 340–353.
17 E. Santos, P. Quaino and W. Schmickler, *Phys. Chem. Chem. Phys.*, 2012, **14**, 11224–11233.
18 S. W. Boettcher and Y. Surendranath, *Nat. Catal.*, 2021, **4**, 4–5.
19 H. N. Nong, L. J. Falling, A. Bergmann, M. Klingenhof, H. P. Tran, C. Spori, R. Mom, J. Timoshenko, G. Zichittella, A. Knop-Gericke, S. Piccinin, J. Perez-Ramirez, B. R. Cuenya, R. Schlogl, P. Strasser, D. Teschner and T. E. Jones, *Nature*, 2020, **587**, 408–413.
20 K. M. Lodaya, B. Y. Tang, R. P. Bisbey, S. Weng, K. S. Westendorff, W. L. Toh, J. Ryu, Y. Román-Leshkov and Y. Surendranath, *Nat. Catal.*, 2024, **7**, 262–272.
21 J. Ryu, D. T. Bregante, W. C. Howland, R. P. Bisbey, C. J. Kaminsky and Y. Surendranath, *Nat. Catal.*, 2021, **4**, 742–752.
22 G. Cheng, W. Zhang, A. Jentys, E. E. Ember, O. Y. Gutierrez, Y. Liu and J. A. Lercher, *Nat. Commun.*, 2022, **13**, 7967.
23 J. S. Adams, M. L. Kromer, J. Rodriguez-Lopez and D. W. Flaherty, *J. Am. Chem. Soc.*, 2021, **143**, 7940–7957.
24 H. C. S. Eckstrom, *Chem. Rev.*, 1939, **24**, 367–414.
25 L. Onsager, *J. Chem. Phys.*, 1934, **2**, 599–615.
26 S. Z. Oener, M. J. Foster and S. W. Boettcher, *Science*, 2020, **369**, 1099–1103.
27 L. Chen, Q. Xu, S. Z. Oener, K. Fabrizio and S. W. Boettcher, *Nat. Commun.*, 2022, **13**, 3846.
28 L. Chen, Q. Xu and S. W. Boettcher, *Joule*, 2023, **7**, 1867–1886.
29 C. G. Rodellar, J. M. Gisbert-Gonzalez, F. Sarabia, B. Roldan Cuenya and S. Z. Oener, *Nat. Energy*, 2024, **9**, 548–558.
30 É. Lucas, J. C. Bui, T. N. Stovall, M. Hwang, K. Wang, E. R. Dunn, E. Spickermann, L. Shiau, A. Kusoglu, A. Z. Weber, A. T. Bell, S. Ardo, H. A. Atwater and C. Xiang, *ACS Energy Lett.*, 2024, **9**, 5596–5605.
31 J. C. Bui, E. W. Lees, D. H. Marin, T. N. Stovall, L. Chen, A. Kusoglu, A. C. Nielander, T. F. Jaramillo, S. W. Boettcher, A. T. Bell and A. Z. Weber, *Nat. Chem. Eng.*, 2024, **1**, 45–60.
32 J. C. Bui, K. R. M. Corpus, A. T. Bell and A. Z. Weber, *J. Phys. Chem. C*, 2021, **125**, 24974–24987.
33 J. C. Bui, I. Digdaya, C. Xiang, A. T. Bell and A. Z. Weber, *ACS Appl. Mater. Interfaces*, 2020, **12**, 52509–52526.
34 *Proc. R. Soc. London, Ser. A*, 1997, **247**, 505–533.
35 F. H. Stillinger and C. W. David, *J. Chem. Phys.*, 1978, **69**, 1473–1484.
36 J. Lentz and S. H. Garofalini, *Phys. Chem. Chem. Phys.*, 2018, **20**, 16414–16427.
37 D. Strmcnik, P. P. Lopes, B. Genorio, V. R. Stamenkovic and N. M. Markovic, *Nano Energy*, 2016, **29**, 29–36.
38 N. Dubouis and A. Grimaud, *Chem. Sci.*, 2019, **10**, 9165–9181.
39 J. A. Gauthier, Z. Lin, M. Head-Gordon and A. T. Bell, *ACS Energy Lett.*, 2022, **7**, 1679–1686.
40 S. Roy and A. K. Tiwari, *J. Phys. Chem. C*, 2021, **125**, 13819–13835.
41 D. Lu and G. A. Voth, *J. Am. Chem. Soc.*, 1998, **120**, 4006–4014.
42 S. Sasmal, L. Chen, P. V. Sarma, O. T. Vulpin, C. R. Simons, K. M. Wells, R. J. Spontak and S. W. Boettcher, *Nat. Mater.*, 2024, **23**, 1421–1427.
43 K. Xie, R. K. Miao, A. Ozden, S. Liu, Z. Chen, C. T. Dinh, J. E. Huang, Q. Xu, C. M. Gabardo, G. Lee, J. P. Edwards, C. P. O'Brien, S. W. Boettcher, D. Sinton and E. H. Sargent, *Nat. Commun.*, 2022, **13**, 3609.
44 H. Song, C. A. Fernández, A. Venkataraman, V. D. Brandão, S. S. Dhingra, S. S. Arora, S. S. Bhargava, C. M. Villa, C. Sievers, S. Nair and M. C. Hatzell, *ACS Appl. Energy Mater.*, 2024, **7**, 1224–1233.
45 B. Siritanaratkul, M. Förster, F. Greenwell, P. K. Sharma, E. H. Yu and A. J. Cowan, *J. Am. Chem. Soc.*, 2022, **144**, 7551–7556.
46 M. Hesselmann, J. K. Lee, S. Chae, A. Tricker, R. G. Keller, M. Wessling, J. Su, D. Kushner, A. Z. Weber and X. Peng, *ACS Appl. Mater. Interfaces*, 2024, **16**, 24649–24659.
47 J. C. Bui, É. Lucas, E. W. Lees, A. K. Liu, H. A. Atwater, C. Xiang, A. T. Bell and A. Z. Weber, *Energy Environ. Sci.*, 2023, **16**, 5076–5095.
48 S. Vallejo Castaño, Q. Shu, M. Shi, R. Blauw, P. Loldrup Fosbøl, P. Kuntke, M. Tedesco and H. V. M. Hamelers, *Chem. Eng. J.*, 2024, 488.
49 I. A. Digdaya, I. Sullivan, M. Lin, L. Han, W. H. Cheng, H. A. Atwater and C. Xiang, *Nat. Commun.*, 2020, **11**, 4412.
50 P. K. Giesbrecht and M. S. Freund, *Chem. Mater.*, 2020, **32**, 8060–8090.
51 Z. Yan, L. Zhu, Y. C. Li, R. J. Wycisk, P. N. Pintauro, M. A. Hickner and T. E. Mallouk, *Energy Environ. Sci.*, 2018, **11**, 2235–2245.
52 Z. Yan, J. L. Hitt, Z. Zeng, M. A. Hickner and T. E. Mallouk, *Nat. Chem.*, 2021, **13**, 33–40.
53 E. Yamamoto, T. Gao, L. Xiao, K. Kopera, S. Marth, H. Park, C. Bae, M. Osada and T. E. Mallouk, *J. Am. Chem. Soc.*, 2025, **147**, 14270–14279.
54 M. B. McDonald and M. S. Freund, *ACS Appl. Mater. Interfaces*, 2014, **6**, 13790–13797.
55 T. Gao, L. Schulte, L. Xiao, E. Yamamoto, A. S. Metlay, C. J. Sheehan, S. Marth, H. Park, S. Sasmal, F. J. Galang, C. Bae, A. Z. Weber, S. W. Boettcher and T. E. Mallouk, *Adv. Energy Mater.*, 2024, 15.
56 S. Mafé, P. Ramírez and A. Alcaraz, *Chem. Phys. Lett.*, 1998, **294**, 406–412.

57 N. P. Craig, Electrochemical Behaviour of Bipolar Membranes, PhD thesis, UC Berkeley, 2013, https://escholarship.org/uc/item/8058x81t#author.
58 Z. Jiang, P. P. Bazianos, Z. Yan and A. M. Rappe, *ACS Catal.*, 2023, **13**, 7079–7086.
59 N. K. Razdan, T. C. Lin and A. Bhan, *Chem. Rev.*, 2023, **123**, 2950–3006.
60 B. Lv, K. Xu, C. Fang, Q. Yang, N. Li, P. Jiang and W. Wang, *J. Chem. Res.*, 2022, 46.
61 J. Newman and K. E. Thomas-Alyea, *Electrochemical Systems*, John Wiley and Sons, Inc., 2004.
62 A. M. Smith, A. A. Lee and S. Perkin, *J. Phys. Chem. Lett.*, 2016, **7**, 2157–2163.
63 Y. Litman and A. Michaelides, *J. Am. Chem. Soc.*, 2025, **147**, 44885–44894.
64 N. Danilovic, R. Subbaraman, D. Strmcnik, K. C. Chang, A. P. Paulikas, V. R. Stamenkovic and N. M. Markovic, *Angew. Chem., Int. Ed.*, 2012, **51**, 12495–12498.
65 X. Chen, X. T. Wang, J. B. Le, S. M. Li, X. Wang, Y. J. Zhang, P. Radjenovic, Y. Zhao, Y. H. Wang, X. M. Lin, J. C. Dong and J. F. Li, *Nat. Commun.*, 2023, **14**, 5289.
66 Y. Wang, J. Zhang, J. Zhao, Y. Wei, S. Chen, H. Zhao, Y. Su, S. Ding and C. Xiao, *ACS Catal.*, 2024, **14**, 3457–3465.
67 J.-M. McGregor, J. T. Bender, A. S. Petersen, L. Cañada, J. Rossmeisl, J. F. Brennecke and J. Resasco, *Nat. Catal.*, 2025, **8**, 79–91.
68 I. Ledezma-Yanez, W. D. Z. Wallace, P. Sebastián-Pascual, V. Climent, J. M. Feliu and M. T. M. Koper, *Nat. Energy*, 2017, 2.
69 Y. Litman and A. Michaelides, *arXiv*, preprint, arXiv. 2506.11734, 2025, DOI: 10.48550/arXiv.2506.11734.
70 R. A. van Santen, M. Neurock and S. G. Shetty, *Chem. Rev.*, 2010, **110**, 2005–2048.
71 P. L. Jordan, H. N. Raum, S. Groger and U. Weininger, *JACS Au*, 2025, **5**, 2334–2341.